Complex vector gain-based annealer for minimizing *XY* Hamiltonians

James S. Cummins and Natalia G. Berloff*

Department of Applied Mathematics and Theoretical Physics, University of Cambridge, Wilberforce Road, Cambridge, CB3 0WA, United Kingdom

(Received 25 December 2024; revised 24 November 2025; accepted 20 January 2026; published 25 March 2026)

This paper is a contribution to the Physical Review Applied collection titled Physics-Inspired Computing.

We present the complex vector gain-based annealer (CVGA), an analog computing platform designed to overcome energy barriers in *XY* Hamiltonians through a higher-dimensional representation. Traditional gain-based solvers using optical or photonic hardware typically represent each *XY* spin with a single complex field. These solvers often struggle with large energy barriers in complex landscapes, leading to relaxation into excited states. CVGA addresses these limitations by using two complex fields to represent each *XY* spin and dynamically evolving the energy landscape through time-dependent annealing. Operating in a higher-dimensional space, CVGA bridges energy barriers in this expanded space during the continuous phase evolution, thus avoiding entrapment in local minima. We introduce several graph structures that pose challenges for *XY* minimization and use them to benchmark CVGA against single-dimension *XY* solvers, highlighting the benefits of higher-dimensional operation.

DOI: 10.1103/lpwn-t7sv

I. INTRODUCTION

The growing complexity and sheer scale of modern scientific and industrial computing tasks are pushing us to look beyond traditional von Neumann architectures for solutions to hard optimization problems. These architectures, which dominate computing today, rely on a clear separation between memory and processing and execute tasks in a step-by-step manner. While traditional computing has been reliable for decades, it is starting to fall behind when it comes to the needs of today's specialized applications—particularly those that demand high speed, energy efficiency, and scalability. As areas such as machine learning, big data analysis, and real-time processing continue to grow, the limitations of the von Neumann approach have become more evident, creating a bottleneck that is increasingly difficult to overcome. This is where analog systems come in, offering a tailored approach to specific types of computing tasks, bypassing the constraints of conventional architectures.

Physics-inspired analog machines have been proposed using various platforms, such as superconducting qubits [1–3], optical parametric oscillators [4–8], memristors [9], lasers [10–12], photonic systems [13,14], trapped ions [15], polariton condensates [16,17], photon condensates [18], and surface acoustic waves [19]. These specialized physical machines minimize programmable spin Hamiltonians, where the couplings between spins given by the interaction matrix $\mathbf{J}$ are designed such that the global minimum corresponds to the optimal solution of a combinatorial optimization problem. Problems such as number partitioning, the traveling salesman problem, graph coloring, spin glass systems, the knapsack problem, binary linear programming, graph partitioning, and the max-cut problem can be mapped to spin Hamiltonians [20–22]. Further applications include machine learning [23–26], financial markets [27], and portfolio optimization [28]. Most proposed physical analog machines use one-dimensional ("hard" or "soft") spins as variables in the discrete binary Ising Hamiltonian $H_I = -\sum_{i,j}^{N} J_{ij}\,\mathbf{s}_i\mathbf{s}_j$ with $\mathbf{s}_i = \pm 1$, or the continuous *XY* Hamiltonian $H_{XY} = -\sum_{i,j}^{N} J_{ij}\,\mathbf{s}_i \cdot \mathbf{s}_j$, where $\mathbf{s}_i = (\cos\theta_i, \sin\theta_i)$, $\theta_i \in [0, 2\pi)$, and N is the number of spins.

The *XY* model describes a system of spins constrained to rotate within a plane, each possessing a continuous degree of freedom characterized by a phase θ_i relative to a fixed axis. Interactions between phases give rise to a rich array of dynamics, including vortices and Berezinskii-Kosterlitz-Thouless transitions [29]. Originally developed for statistical mechanics and condensed matter physics, the *XY* model has found extensive applications in various physical systems where rotational symmetry is essential. Notably, it applies to superfluidity and superconductivity [30],

*Contact author: n.g.berloff@damtp.cam.ac.uk

Published by the American Physical Society under the terms of the Creative Commons Attribution 4.0 International license. Further distribution of this work must maintain attribution to the author(s) and the published article's title, journal citation, and DOI.

cosmology [31], nematic liquid crystals [32], magnetic nanoparticle ensembles [33], protein folding [34], and phase retrieval problems [35].

Gain-based minimizers use soft-spin bifurcation dynamics via Andronov-Hopf bifurcations to minimize spin Hamiltonians [36]. The increased dimensionality offered by soft-spin models reduces energy barriers present in classical hard-spin Hamiltonians by representing fixed spin amplitudes as continuous variables [37]. We recently proposed the vector Ising spin annealer (VISA) as an Ising minimization model capable of overcoming obstacles in solving combinatorial optimization problems [38]. By using three soft modes to represent the vector components of an Ising spin, VISA bridges minima separated by significant energy barriers in complex energy landscapes. VISA uses real-valued soft spins, which can, for example, represent the optical parametric oscillator quadrature in coherent Ising machines.

In this paper, we propose using multiple vector components to represent the spins in networks of complex-valued fields ψ_i, which are known to minimize XY and Ising Hamiltonians in gain-based systems [39]. The Stuart-Landau equation, which governs the dynamics of one-dimensional complex oscillators ψ_i in gain-based networks, is given by

$$\dot{\psi}_i = \left(\gamma_i - |\psi_i|^2\right)\psi_i + \alpha \sum_j J_{ij}\psi_j, \tag{1}$$

where we introduced a regulation parameter $\alpha > 0$ and the effective gain rate γ_i is individually dynamically adjusted through a feedback mechanism,

$$\dot{\gamma}_i = \varepsilon\left(1 - |\psi_i|^2\right), \tag{2}$$

which can be implemented via optical delay lines for laser systems, or by spatial light modulators (SLMs) for polariton condensates [17]; see also Appendix A. The dynamical equation (1) can be written as $\dot{\psi}_i = -\partial H/\partial\psi_i^*$, which describes the process of gradient descent to the minima of the loss function

$$H = \frac{1}{2}\sum_{i=1}^{N}\left(\gamma_i - |\psi_i|^2\right)^2 - \frac{\alpha}{2}\sum_{i,j}^{N} J_{ij}\left(\psi_i\psi_j^* + \psi_i^*\psi_j\right), \tag{3}$$

where $\dot{\gamma}_i = 0$ for all i at the threshold steady state. By representing each oscillator in its polar form as $\psi_i = r_i\exp(i\theta_i)$, we can decompose Eq. (1) into real and imaginary parts to get equations for the time evolution of the amplitude r_i and the phase θ_i as

$$\dot{r}_i = \gamma_i r_i - r_i^3 + \alpha\sum_j J_{ij} r_j\cos\left(\theta_i - \theta_j\right), \tag{4}$$

$$\dot{\theta}_i = -\alpha\sum_j J_{ij}\frac{r_j}{r_i}\sin\left(\theta_i - \theta_j\right). \tag{5}$$

A discussion of how the same gain-based framework specializes to Ising and general q-state models by restricting the allowed phase subspace is given in Appendix B. Starting from below the steady-state threshold in the vacuum state $r_i = 0$, all oscillators are pumped equally. Then, depending on the structure of $\mathbf{J}$, nonzero amplitudes emerge at different rates for each oscillator as the pumping intensity increases. The feedback mechanism of Eq. (2) adjusts each oscillator so that they all reach equal amplitudes at the steady-state threshold.

Only under the condition of equal amplitudes at the steady state will Eq. (5) reach the minimum of the XY Hamiltonian. The sum of the steady states of Eq. (4) gives $N = \sum_{i=1}^{N}\gamma_i + \alpha\sum_{i,j}J_{ij}\cos\left(\theta_i - \theta_j\right)$, so the global minimum of the XY model corresponds to the smallest effective injection $\sum_i\gamma_i$. Close to the threshold, Eq. (5) becomes fully analogous to the Kuramoto model

$$\dot{\theta}_i = -\alpha\sum_{j=1}^{N} J_{ij}\sin\left(\theta_i - \theta_j\right). \tag{6}$$

The prefactor α can be absorbed into a rescaling of time $\tau = \alpha t$, so it does not affect the fixed points or their basins of attraction; in practice we set $\alpha = 1$ and choose the integration horizon T large enough to ensure convergence in all Kuramoto runs. Equation (1) can be adapted to minimize Ising Hamiltonians by restricting the state space of the phase, which we detail in Appendix B.

Gain-based systems described by Eq. (1) can still settle in local minima during amplitude bifurcation, which limits the probability of finding the global minimum. To combat this, we introduce the complex vector gain-based annealer (CVGA), which exploits the advantages of extended spatial dimensions. In this model, continuous XY spins are represented as complex-valued vectors in two-dimensional vector space $\boldsymbol{\Psi}_i \in \mathbb{C}^2$. The increased dimension over typical one-dimensional spins allows the barriers between minima to be overcome effectively.

In this paper we propose, to our knowledge, a new approach to minimizing XY Hamiltonians that uses the ultrafast energy-efficient architecture of photonics-based analog machines. In Sec. II, we formalize CVGA, and provide expressions for each term in its composite Hamiltonian. In Sec. III, we use the Kuramoto model to investigate the difficulty of various XY minimization problems. This allows us to identify suitably hard benchmark problems to test CVGA and existing XY minimization algorithms, as recovering the global minimum of these problems is nontrivial. Lastly, in Sec. IV we compare CVGA's dynamics with those of the one-dimensional Stuart-Landau network and with other continuous-variable approaches, including

the spin-vector Langevin (SVL) and Kuramoto models. We contrast these methods by their ground-state recovery probabilities and by the distributions of recovered states.

II. COMPLEX VECTOR GAIN-BASED ANNEALER

The CVGA model operates through a system of N two-dimensional complex-field vectors $\boldsymbol{\Psi}_i = (\psi_i^{(1)} = r_i^{(1)} e^{i\theta_i^{(1)}}, \psi_i^{(2)} = r_i^{(2)} e^{i\theta_i^{(2)}})$. It uses annealing, symmetry-breaking bifurcation, gradient descent, and mode selection to drive the system to the global minimum. The Hamiltonian is the sum of three terms $H = H_1 + \alpha H_2 + H_3$, where

$$H_1 = \frac{1}{2}\sum_{i=1}^{N}\left(\gamma_i(t) - ||\boldsymbol{\Psi}_i||_2^2\right)^2, \tag{7}$$

$$H_2 = -\frac{1}{2}\sum_{i,j}^{N} J_{ij}\left(\boldsymbol{\Psi}_i \cdot \boldsymbol{\Psi}_j^* + \boldsymbol{\Psi}_i^* \cdot \boldsymbol{\Psi}_j\right), \tag{8}$$

$$H_3 = -\frac{1}{2}P(t)\sum_{i,j=1}^{N}\left(\boldsymbol{\Psi}_j \odot \boldsymbol{\Psi}_i^*\right)\cdot\left[\mathbf{Q}(\boldsymbol{\Psi}_j^* \odot \boldsymbol{\Psi}_i)\right]. \tag{9}$$

Here $\odot$ indicates elementwise multiplication, and $\mathbf{Q}$ is a 2×2 permutation matrix given by $\mathbf{Q} = \left(\begin{smallmatrix} 0 & 1 \\ 1 & 0 \end{smallmatrix}\right)$. As the effective gain $\gamma_i(t)$ increases with time t from negative (effective losses) to positive values, H_1 evolves from a convex function with its minimum at $||\boldsymbol{\Psi}_i||_2^2 = 0$ for all i to one that favors finite (nonzero) amplitudes. Writing the complex vectors in H_2 using their polar coordinates, we obtain

$$H_2 = -\sum_{i,j} J_{ij}\left(r_i^{(1)} r_j^{(1)} \cos\theta_{ij}^{(1)} + r_i^{(2)} r_j^{(2)} \cos\theta_{ij}^{(2)}\right), \tag{10}$$

where we define $\theta_{ij}^{(k)} \equiv \theta_i^{(k)} - \theta_j^{(k)}$. Equation (10) is analogous to the second term on the right-hand side of Eq. (3), but now we have two terms corresponding to the two dimensions in the complex vector space that CVGA operates in. The effective gain is subject to the feedback governed by $\dot{\gamma}_i = \varepsilon(2 - ||\boldsymbol{\Psi}_i||_2^2)$. This drives the effective gain rates from below and brings each component amplitude to unity ($\|\boldsymbol{\Psi}_i\|_2^2 = 2$) at the steady state. Finally, H_3 is a penalty term with time-dependent magnitude $P(t)$ that enforces agreement of the phase differences in each dimension. This 4-local penalty term, expressed in Eq. (9), can be expanded into its constituent complex fields, which transforms H_3 to

$$H_3 = -\frac{1}{2}P(t)\sum_{i,j}\psi_i^{(1)}\psi_i^{(2)*}\psi_j^{(1)*}\psi_j^{(2)} + \text{c.c.} \tag{11}$$

When the complex oscillators have equal unit-valued amplitudes, $||\boldsymbol{\Psi}_i||_2^2 = 2$ for all i, H_3 becomes

$$H_3 = -P(t)\sum_{i,j}\cos\left(\theta_{ij}^{(1)} - \theta_{ij}^{(2)}\right), \tag{12}$$

which is minimized when $\theta_{ij}^{(1)} = \theta_{ij}^{(2)}$ for all pairs (i,j). As $P(t)$ increases from $P(0) = 0$ to sufficiently large $P(T) > 0$ at $t = T$, the phase differences $\theta_{ij}^{(1)}$ and $\theta_{ij}^{(2)}$ become equal. Therefore, up to a global phase offset, $\theta_i^{(1)} = \theta_i^{(2)}$. At the end of the annealing protocol, the target XY Hamiltonian H_{XY} is minimized. We evolve the CVGA Hamiltonian H using gradient descent while simultaneously annealing the parameters γ_i and $P(t)$. Therefore, for each oscillator i, the governing equation $\dot{\boldsymbol{\Psi}}_i = -\nabla_i H$ is given by

$$\dot{\boldsymbol{\Psi}}_i = \boldsymbol{\Psi}_i\left(\gamma_i(t) - ||\boldsymbol{\Psi}_i||_2^2\right) + \alpha\sum_{j=1}^{N} J_{ij}\boldsymbol{\Psi}_j + P(t)\sum_{j=1}^{N}\boldsymbol{\Psi}_j \odot \left[\mathbf{Q}(\boldsymbol{\Psi}_j^* \odot \boldsymbol{\Psi}_i)\right]. \tag{13}$$

The operation of CVGA relies on gradient descent on an annealed energy landscape. To experimentally realize Eq. (13), modern photonic platforms—such as laser arrays, SLMs, and integrated photonic circuits—can encode the two-component complex vectors $\boldsymbol{\Psi}_i = (\psi_i^{(1)}, \psi_i^{(2)})$. Each component may be represented by the amplitude and phase of light in distinct colocated modes (e.g., polarizations, frequency channels, or waveguides), while the coupling matrix J_{ij} is implemented with the use of programmable waveguide meshes or SLM-based optical fan-out and combine networks. Gain regulation and the effective gain parameter $\gamma_i(t)$ are controlled by pump modulation or optical amplifiers, and real-time adjustments are achieved through electro-optic modulators or SLMs. Annealing of $\gamma_i(t)$ or α proceeds over many cavity lifetimes (from nanoseconds to microseconds or longer, depending on the platform and electronics), and the resulting fields are read out with the use of phase-sensitive cameras or interferometers to obtain the minimized XY configuration.

Within this general architecture, the four-body penalty H_3 requires no exotic many-body optics. It can be generated with the use of standard $\chi^{(3)}$ nonlinear and measurement-feedback elements already present in photonic XY and Ising machines. Each XY spin is represented by two colocated optical modes that experience local Kerr or cross-phase-modulation nonlinearities. Interference of the pairs of modes from all sites on a beam splitter or waveguide network yields a collective "overlap" mode $O = \sum_i \psi_i^{(1)}\psi_i^{(2)*}$, and a single nonlinear element acting on this mode produces an effective term $-P'(t)|O|^2$. When

rewritten in terms of the site amplitudes, this contribution becomes equivalent—up to a rescaling of $P(t)$—to the global four-body interaction of Eq. (11), enforcing alignment of phase differences between the two components [see Eq. (12)]. Such global quartic couplings between collective optical modes are routinely implemented in $\chi^{(3)}$ integrated-photonics platforms and polariton-condensate networks used for analog spin minimization [16,40–44]. In hybrid digital-analog architectures, the same overlap mode can be measured interferometrically, and a pump modulation proportional to $-P(t)O$ can be fed back, consistent with the Microsoft analog optical computer approach to nonlocal couplings [42,43]. Crucially, CVGA requires only this *uniform, graph-independent* penalty term; all instance programmability remains in the two-body couplings J_{ij}, so realizing H_3 introduces no additional instance-specific hardware complexity.

A complementary and fully linear-optical mechanism for realizing the same class of four-body interactions was recently proposed. A single passive optical relay placed between two SLM-programmable planes can implement native k-body interactions by routing products of optical fields through an additional Fourier-plane degree of freedom [45]. For $k = 4$, this relay-based architecture produces global quartic couplings of precisely the form required by H_3, using only linear optics together with standard optical fan-in and fan-out and phase-programmable masks. Thus, both the standard $\chi^{(3)}$ route and the relay-based route provide concrete and experimentally feasible ways of implementing the uniform four-body penalty of Eq. (9), reinforcing that CVGA requires no exotic, instance-dependent hardware. Its sole nontrivial interaction is a graph-independent quartic term that can be generated either by mature $\chi^{(3)}$ platforms or by a single passive optical component in a programmable free-space system.

A simple analytic illustration of how the additional vector component in CVGA lowers barriers on a frustrated instance—a single antiferromagnetic triangle—is provided in Appendix F.

Although we present CVGA in the context of XY Hamiltonians, the underlying mechanism is not limited to two-body phase interactions. The approach relies on two structural elements: (1) embedding each spin in a higher-dimensional soft vector space, which introduces low-energy directions absent in single-component models, and (2) a time-dependent locking penalty that projects the system back onto the target spin manifold. This combination is readily adaptable to other classical Hamiltonians. As discussed in Appendix B, resonant forcing can restrict the allowed phases to $\{0, \pi\}$ or, more generally, to $\{2\pi m/q\}$, yielding Ising, Potts, and q-state clock models. More complicated k-local couplings may be incorporated by introducing additional vector components or auxiliary penalty terms that enforce multispin constraints, analogous to slack variables in digital or quantum encodings. While a detailed exploration of these generalizations is beyond the scope of this work, the CVGA architecture is naturally extensible to broader families of classical spin Hamiltonians.

In the next section, we seek suitable graph structures for benchmarking CVGA and alternative algorithms for XY Hamiltonian minimization. For benchmarking, we choose graphs with analytically tractable yet nontrivial ground states and energies and whose basins of attraction are small in volume. In this way, simple gradient-based algorithms are expected to falter in recovering the global minimum. Moreover, we seek technologically feasible graphs on analog hardware [44,46,47]. Complex graphs for optimization may contain topological structures resistant to simple local perturbations. In the XY regime, these often arise as domain boundaries or vortices. For domain boundaries, the transformation from the excited state to the ground state requires an entire domain to reverse its chirality, representing a significant energy barrier to be overcome. Therefore, in this case, local perturbations are not enough to bridge local and global minima.

III. GRAPHS FOR *XY* MINIMIZATION

To rigorously test CVGA's capabilities, we select graph types that, due to their complex topologies and high energy barriers, present distinct challenges for gradient-based methods. We consider network graph structures given by the coupling matrix **J**, resulting in nontrivial minimization instances for simple gradient-based solvers. To do this, we represent the gradient dynamics by the Kuramoto model [Eq. (6)], as it represents a gradient descent with respect to XY phases θ_i. Moreover, by using the Kuramoto model, we can infer the sizes of the basins of attraction for each locally stable state. This is because, under gradient descent, the system evolves to the the minimum whose basin contains the initial condition.

A. 4-regular Möbius ladder

The 4-regular Möbius ladder network is an unweighted 4-regular circulant graph with antiferromagnetic couplings $J_{ij} \in \{-1, 0\}$ between its N vertices. It is inspired by its 3-regular version, often used as an Ising solver benchmark [37,38,48]; see Appendixes C and D. We consider only cases for which $N/2$ is divisible by 3, in which case the ground state has no frustrations, and any connected spin pair has phase difference $\pm 2\pi/3$. Then, the graphs, illustrated in Figs. 1(a) and 1(b) consist of N triangular bases connected to each other, with the first and last bases joined, creating a periodic circular geometry. For any triangle with nodes i, j, k, we define the chirality $C_{ijk} \in \{0, \pm 1\}$ depending on whether there is a phase winding around these nodes and in which direction. The ground state corresponds to alternating chirality between adjacent triangles. Therefore, we define the excitation parameter D for any 4-regular

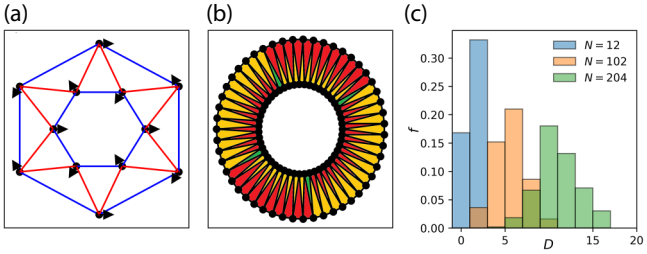


FIG. 1. (a) Ground-state solution, up to a global phase change, for an $N = 12$ 4-regular Möbius ladder graph. In this ground state, every XY spin has a phase difference of $\pm 2\pi/3$ with each of its nearest neighbors. (b) Excited state of an $N = 102$ 4-regular Möbius ladder graph with $D = 4$. Here the phases are not illustrated, and instead color represents the chirality of each triangular base. For a base with indices $\{i,j,k\}$, $C_{ijk} = -1$ is shown in yellow, $C_{ijk} = 1$ in red, and $C_{ijk} = 0$ in green. (c) Frequency density histogram of excitation parameter D for 1000 runs of the Kuramoto model on $N = \{12, 102, 204\}$ 4-regular Möbius ladder graphs. In each run, initial phases $\theta_i(0)$ are chosen uniformly at random from the range $[-\pi, \pi)$, and Eq. (6) is solved with use of the Euler scheme with fixed time step $\Delta t = 0.1$.

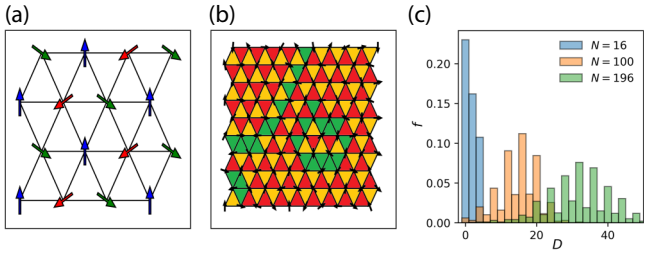


FIG. 2. (a) A ground-state solution for an $N = 4 \times 4$ triangular lattice graph, where every XY spin has a phase difference of $\pm 2\pi/3$ with each of its neighbors. (b) Excited state of an $N = 10 \times 10$ triangular lattice graph. Here the phases are not illustrated, and instead color represents the chirality of each triangular base. For a base with indices $\{i,j,k\}$, $C_{ijk} = -1$ is shown in yellow, $C_{ijk} = +1$ in red, and $C_{ijk} = 0$ in green. Domains are more likely to exist when part of their boundaries are the edges of the triangular lattice since, on these edges, there are no excited (green) triangular bases. This is a consequence of the graph's nonperiodic boundary conditions. (c) Frequency density histogram of excitation parameter D for 1000 runs of the Kuramoto model on $N = \{16, 100, 196\}$ triangular lattice graphs. In each run, initial phases $\theta_i(0)$ are chosen uniformly at random from the range $[-\pi, \pi)$, and Eq. (6) is solved with use of the Euler scheme with fixed time step $\Delta t = 0.1$.

Möbius ladder graph as

$$D = \sum_{\{ijk\} \in \mathcal{T}} \left(1 - |C_{ijk}|\right) \tag{14}$$

to account for excitations that occur as domain boundaries, where $\mathcal{T}$ is the set of vertices for each triangle. This is where triangular bases with zero chirality separate domains with triangular bases of alternating chirality ± 1. Further analytic properties of Möbius ladder graphs, including their circulant structure and ground-state transitions, are summarized in Appendix C.

The frequency density histogram of excitation parameter D for states recovered by the Kuramoto model [Eq. (6)] is shown in Fig. 1(c). Since the system descends to the the minimum whose basin contains the initial condition according to Eq. (6), the histogram represents the volumes of the basins of attraction for each minima. Figure 1(c) shows that as the system size N increases, the volume of the basin of attraction of the ground state decreases as a proportion of the total volume of all basins, and recovery of the ground state by standard gradient descent becomes hard.

B. Triangular lattice

The triangular lattice is a two-dimensional graph consisting of triangles in a regular arrangement. Each of the N vertices corresponds to an XY spin, while edges represent unweighted antiferromagnetic couplings $J_{ij} = -1$. The ground state is recognized by its arrangement of phases, with every XY spin having phase difference $\pm 2\pi/3$ with each of its nearest neighbors. As for 4-regular Möbius ladder graphs, we can use the same excitation parameter D from Eq. (14) to categorize ground and excited states. The frequency density histogram of excitation parameter D for states recovered by the Kuramoto model [Eq. (6)] is shown in Fig. 2(c). As the system size N increases, the number of trials in the histogram bin corresponding to the ground state $D = 0$ decreases.

Taken together, the histograms in Figs. 1(c) and 2(c) provide a natural *classical difficulty metric* for gradient-based XY solvers. The relative height of the $D = 0$ bin directly measures the fraction of phase space (under random initial conditions) that flows to the global minimum under Kuramoto dynamics. As the system size N increases, this bin shrinks dramatically, indicating that the ground-state basin occupies an increasingly small region of configuration space. In this sense, the reduction of the $D = 0$ basin serves as a classical analogue of an "effective gap": when the basin becomes vanishingly small, local methods almost always converge to excited (locally minimal) states. As we show in Sec. IV, CVGA's performance gains are largest precisely in these regimes where the Kuramoto ground-state basin is smallest.

C. Basic Kuratowskian graphs

Basic Kuratowskian graphs are nonplanar subgraphs that appear in every two-dimensional or three-dimensional nonplanar graph. With random couplings $J_{ij} \in \{-1, 0, +1\}$, the Ising problem on these graphs is NP-complete [49], but their continuous XY counterpart has not been extensively

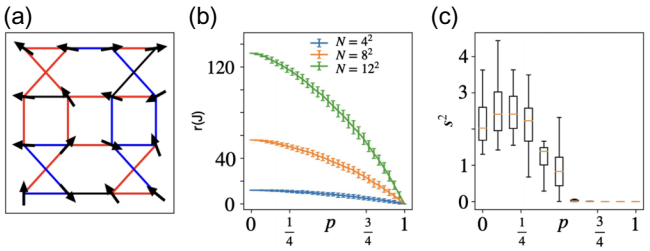


FIG. 3. (a) Example configuration of XY phases on an $N = 4 \times 4$ basic Kuratowskian graph with $p = 0.2$. Unlike the Möbius ladders in Fig. 1(a), this instance contains *randomly assigned* ferromagnetic, antiferromagnetic, and zero couplings $J_{ij} \in \{-1, 0, +1\}$ drawn from Eq. (15), and is therefore *generically frustrated*. As a result, the XY phases do not display the unfrustrated $\pm 2\pi/3$ structure seen in Fig. 1(a). (b) Rank of the coupling matrix $\mathbf{J}$ as a function of the probability parameter p, with each point averaged over 100 Kuratowskian graphs and error bars indicating the standard deviation. (c) Box-plot distributions of sample variance values s^2 for the final-state energies of Eq. (6), obtained from $N = 8 \times 8$ basic Kuratowskian graphs, each box summarizing 100 Kuramoto runs on each of 100 graph instances for the corresponding value of p.

studied. In contrast to the unweighted antiferromagnetic Möbius ladders and triangular lattices, whose ground states are unfrustrated and analytically known, basic Kuratowskian graphs are frustrated by construction: the random mixture of ferromagnetic, antiferromagnetic, and zero couplings generically produces conflicting constraints. The configuration shown in Fig. 3(a) is therefore a typical excited state of such a frustrated instance, rather than a uniform $\pm 2\pi/3$ pattern.

To construct the coupling matrix $\mathbf{J}$ for a basic Kuratowskian graph, we assign each edge in Fig. 3(a) a weight randomly chosen from $W = \{-1, 0, +1\}$. We sample the weights w from the discrete probability mass function $p_W : W \to [0, 1]$, where

$$p_W(w) = \begin{cases} \frac{1}{2}(1-p) & \text{if } w = -1, \\ p & \text{if } w = 0, \\ \frac{1}{2}(1-p) & \text{if } w = +1. \end{cases} \tag{15}$$

Here the parameter $0 \le p \le 1$ in Eq. (15) controls the rank of $\mathbf{J}$ and influences the hardness of the XY minimization problem, as shown in Figs. 3(b) and 3(c). As p increases, the number of nonzero entries in $\mathbf{J}$ decreases, and consequently, the rank decreases. In spatial photonic XY and Ising machines, the rank of the coupling matrix is an important feature of the spin network; indeed, some current implementations are feasible only for low-rank coupling matrices [28].

IV. RESULTS

In this section, we compare CVGA with the one-dimensional spin version, whose Hamiltonian is given by Eq. (3) and governed by the canonical Stuart-Landau network [Eq. (1)], as well as with Kuramoto gradient descent and other methods.

Our goal here is not to identify the fastest possible classical algorithm for each graph family, nor to hyper-optimize every solver in a full time-to-solution sense [50]. Instead, the baseline dynamics [Kuramoto, SVL, one-dimensional Stuart-Landau, and Broyden-Fletcher-Goldfarb-Shanno (BFGS)] are used as conceptual reference methods that explore the same XY energy landscape with different degrees of freedom. The central controlled comparison is between the scalar Stuart-Landau network and its two-component CVGA extension, which we run with identical dimensionless parameters $[\epsilon, \alpha, \gamma(0)]$ and annealing time T, so that the impact of the additional vector component and the locking term H_3 can be isolated. We therefore do not claim that the reported CVGA success probabilities necessarily exceed those of individually optimized Kuramoto, SVL, or Stuart-Landau solvers; a systematic hyperparameter optimization of all baselines would constitute a separate, complementary study. Details of numerical integration, annealing schedules, and the hyperparameters used for each graph size and method are given in Appendix E.

The phase-annealing protocol of CVGA begins with $P(0) = 0$ and gradually increases for $t > 0$, ensuring that the local phase difference in each dimension of the complex-field vector $\boldsymbol{\Psi}_i$ becomes the same. We increase $P(t)$ to a sufficiently large value so that $\theta_{ij}^{(1)} = \theta_{ij}^{(2)}$ holds for every pair (i, j), after which we choose one component from which to extract the XY phases. Under this constraint, each $\theta_i^{(1)}$ is equivalent to $\theta_i^{(2)}$ up to a global phase shift, and hence the choice of component is arbitrary. For simplicity, we choose a monotonically increasing function $P(t)$ with linear time dependence, $P(t) = \beta t$, although other schedules could also be used.

Figure 4 compares CVGA with the one-dimensional Stuart-Landau model of Eq. (3) under equivalent starting conditions on a 4-regular Möbius ladder graph with $N = 36$. It demonstrates that while the scalar version fails to find the ground state ($D = 0$), CVGA leverages multidimensional phase dynamics to recover the global minimum by bridging minima unreachable by the one-dimensional approach.

CVGA allows the system to change phases at a substantially lower energy cost than in the scalar model, because the dynamics may initially move through the additional vector direction to locate low-energy pathways that are inaccessible in a one-dimensional phase space.

To address the question of trade-offs, we first note that CVGA does not modify the asymptotic computational

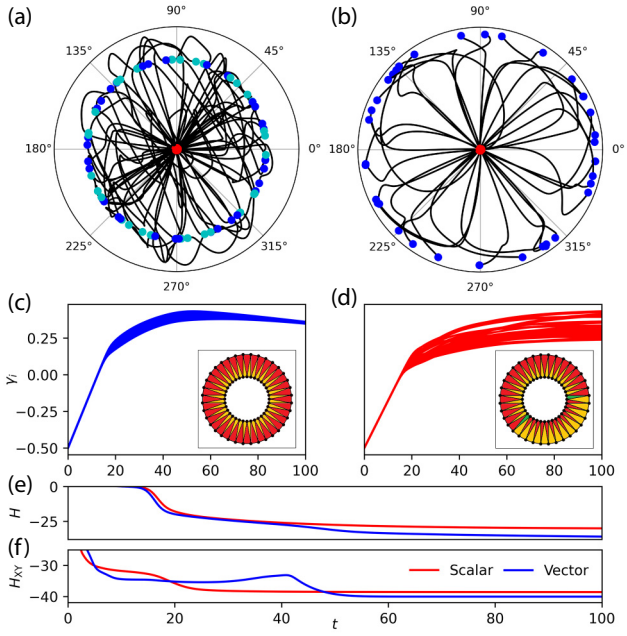


FIG. 4. (a),(b) Comparison of the trajectories of XY spins in the CVGA model and the one-dimensional Stuart-Landau model, respectively, for an $N = 36$ 4-regular Möbius ladder graph. Red circles indicate initial states, while in (a), blue and cyan circles correspond to final states for $\psi_i^{(1)}$ and $\psi_i^{(2)}$. Final states ψ_i in the scalar version [(b)] are highlighted with blue circles. (c),(d) Effective gain γ_i as the systems evolve. CVGA successfully recovers the ground state without frustrations $D = 0$ as seen in the inset in (c), while the one-dimensional scalar version reaches the excited state $D = 2$ shown in the inset in (d). Both systems start from equivalent initial conditions, with the one-dimensional scalar version beginning at $\psi_i(0) = 0.01\exp(ia)$ and CVGA beginning at $\boldsymbol{\Psi}_i(0) = (0.01\exp(i\,a), 0.01\exp(i\,b))$, where a and b are uniformly chosen from the range $[-\pi, \pi)$. (e) Comparison of the CVGA Hamiltonian H against the one-dimensional model [Eq. (3)], and (f) the values of the XY Hamiltonians H_{XY}.

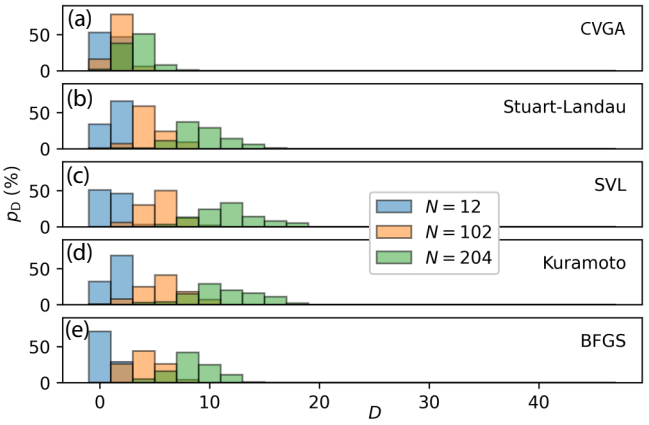


FIG. 5. Probability distribution for recovering a state with excitation parameter D for the CVGA, one-dimensional Stuart-Landau, SVL, Kuramoto, and BFGS methods on $N = 12$ (blue), $N = 102$ (orange), and $N = 204$ (green) 4-regular Möbius ladder graphs. One thousand runs are used to calculate the probability of recovering excitation parameters D for each value of N. Parameter values for CVGA are taken from Table I in Appendix E [51], and so are values for the Stuart-Landau network solver where applicable. For the SVL model, $m = 1.0$, $\xi \sim \mathcal{N}(0, 0.1)$, and $b = 0.9$. In all cases, a fixed time step of $\Delta t = 0.1$ is used with annealing time length $T = 1000$.

scaling of gain-based solvers. For N spins and M nonzero couplings, each integration step of the one-dimensional Stuart-Landau network [Eq. (1)] requires $\mathcal{O}(M)$ operations. CVGA adds a second complex component and the structured contraction appearing in H_3 [Eq. (9)], but all operations remain linear in M. Consequently,

$$C_{\mathrm{CVGA}(N,M)} = c\,\mathcal{O}(M),$$

with c a constant factor of order 2-3 depending on implementation. Since all solvers are integrated over the same annealing time T, the total time to solution differs only by this fixed multiplicative overhead. In return, CVGA achieves much higher ground-state recovery probabilities than the scalar network (Figs. 5–7), thereby *reducing* the expected time to solution when runs are repeated until success. From an analog-hardware perspective, the additional degree of freedom corresponds simply to two colocated optical modes per site, so the hardware overhead is likewise constant. CVGA thus trades a small constant-factor cost for a substantial increase in success probability without altering the fundamental computational scaling.

The origin of this improvement can be viewed in terms of barrier relocation. As shown explicitly in Appendix F, on the smallest frustrated XY instance—the antiferromagnetic triangle—the fixed scalar barrier ΔE_{XY} separating the two chiral ground states is replaced by a CVGA barrier of order $P(t)$ during early annealing. Because $P(t)$ begins at zero and increases only gradually, the system can flip between chiral sectors at parametrically lower cost than in the scalar model.

A complementary viewpoint comes from examining the local curvature of the CVGA energy landscape. Focusing on the phase degrees of freedom and assuming unit amplitudes, we expand $H_2 + H_3$ [Eqs. (10) and (12)] to second order around a configuration with $\theta_i^{(1)} \simeq \theta_i^{(2)}$. By our introducing average and difference variables

$$\phi_i = \frac{\theta_i^{(1)} + \theta_i^{(2)}}{2}, \qquad \delta_i = \theta_i^{(1)} - \theta_i^{(2)},$$

the Hessian becomes approximately block-diagonal. The ϕ sector reproduces the ordinary XY stiffness, matching the Hessian of the scalar model evaluated at the same point. By contrast, the δ sector is dominated by the locking term H_3: it contributes a discrete Laplacian in the δ_i, whose eigenvalues scale as $P(t)$, shifting the curvature of all δ modes upward by $\mathcal{O}(P(t))$. At small $P(t)$, these δ directions are therefore extremely soft; the system can move along them

to transition between competing chiral sectors at very low energetic cost. As $P(t)$ increases, these modes stiffen and the two components lock into a single XY configuration.

This soft-mode structure provides a Hessian-level picture of CVGA's mechanism: the protocol initially exploits nearly flat directions in the extended vector space to bypass otherwise prohibitive barriers, and then gradually opens a tunable "classical gap" in the δ sector as the locking penalty grows.

In addition, we compare CVGA with the SVL model, which was proposed as a classical analogue of a quantum annealing description using stochastic Langevin time evolution governed by the fluctuation-dissipation theorem [52]. The SVL model is based on the time-dependent Hamiltonian used in quantum annealing $H(t) = A(t)H_0 + B(t)H_\mathrm{P}$, where the initial Hamiltonian is $H_0 = -\sum_i \sigma_i^x$. We choose the problem Hamiltonian so that it maps to the XY Hamiltonian as $H_\mathrm{P} = -\sum_{i,j} J_{ij}(\sigma_i^x\sigma_j^x + \sigma_i^z\sigma_j^z)$, with Pauli operator $\boldsymbol{\sigma}_i$ acting on the ith variable. Real annealing functions satisfy boundary conditions $A(0) = B(T) = 1$ and $A(T) = B(0) = 0$, where T is the temporal length of the annealing schedule. If the rate of change of the functions is slow enough, the system stays in the ground state of the instantaneous Hamiltonian so that at $t = T$ the XY Hamiltonian is minimized. The SVL model replaces Pauli operators with real functions of continuous angle $\sigma_i^z \to \sin\theta_i$, $\sigma_i^x \to \cos\theta_i$, and is therefore a classical annealing Hamiltonian using continuous-valued phases θ_i. SVL dynamics is described by a system of coupled stochastic equations:

$$m\ddot{\theta}_i + b\dot{\theta}_i + \frac{\partial H(\theta)}{\partial \theta_i} + \xi_i(t) = 0, \tag{16}$$

where m is the effective mass, b is the damping constant, and $\xi_i(t)$ is independent and identically distributed Gaussian noise. For quadratic unconstrained continuous optimization, such as minimizing the XY model, the gradient term in Eq. (16) is

$$\frac{\partial H(\theta)}{\partial \theta_i} = A(t)\sin\theta_i + B(t)\sum_{j=1} J_{ij}\sin(\theta_i - \theta_j), \tag{17}$$

which in conjunction with the fluctuation-dissipation relations $\langle \xi_i(t)\rangle = 0$ and $\langle \xi_i(t)\xi_j(t')\rangle = \delta_{ij}\delta(t-t')$, gives $2N$ stochastic differential equations: $\mathrm{d}\theta_i = (p_i/m)\mathrm{d}t$ and

$$\mathrm{d}p_i = -\left(\frac{\partial H}{\partial \theta_i} + bp_i/m\right)\mathrm{d}t + \mathrm{d}W_i, \tag{18}$$

where $\mathrm{d}W_i$ represents a real-valued continuous-time stochastic Wiener process [52].

CVGA distinguishes itself from one-dimensional Stuart-Landau networks, the SVL model, and the Kuramoto model through its gain-based annealing strategy in higher-dimensional spaces. In Figs. 5 and 6, we compare CVGA with these models and the BFGS algorithm on 4-regular Möbius ladder graphs and triangular lattice graphs, respectively. The BFGS algorithm is a classical quasi-Newton-method for unconstrained nonlinear optimization that approximates the Hessian matrix to guide the search for a local minimum.

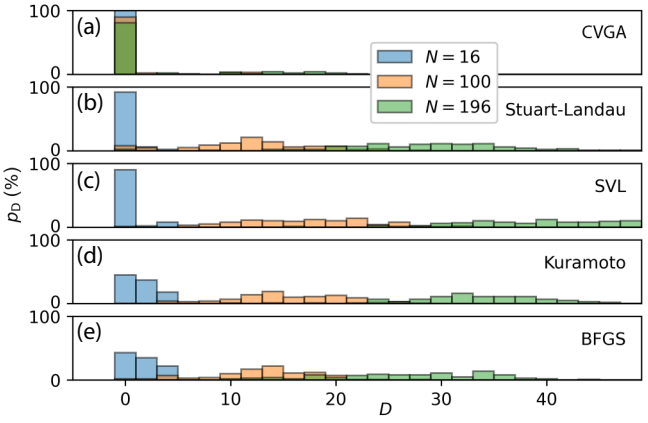


FIG. 6. Probability distribution for recovering a state with excitation parameter D for the CVGA, one-dimensional Stuart-Landau, SVL, Kuramoto, and BFGS methods on $N = 16$ (blue), $N = 100$ (orange), and $N = 194$ (green) triangular lattice graphs. One thousand runs starting from random initial conditions are used to calculate the probability for each method and for each value of N.

By leveraging a multidimensional approach, the CVGA model recovers the ground state ($D = 0$) of 4-regular Möbius ladder and triangular lattice graphs more often than any of the methods with which it is compared. As a result, the distribution of excitations D for CVGA is skewed closer to $D = 0$ for all tested values of N, compared with the single-dimension Stuart-Landau network, and this effect becomes more pronounced as N increases. While the annealing schedules used in these approaches and in the SVL model demonstrate efficient convergence to low-energy solutions compared with the Kuramoto model and the BFGS algorithm, CVGA's higher dimensionality enables XY spins to traverse paths connecting minima and converge to the ground state. This increases system robustness, making the final system less sensitive to the initial conditions.

Next we consider basic Kuratowskian graphs, which exhibit significant difficulty for standard gradient descent methods, as illustrated in Fig. 3 for small values of the parameter p. However, the randomness of the couplings can introduce statistical convergence issues for small sample sizes. Despite this, graphs with random couplings are popular for benchmarking physical simulators [53–55].

Because basic Kuratowskian graph instances do not have analytically known ground states, we use the

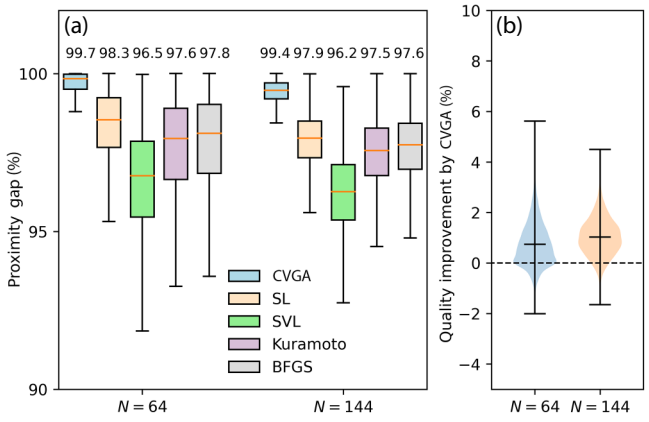


FIG. 7. (a) Proximity gap box plots for each method [CVGA, Stuart-Landau (SL), SVL, Kuramoto, BFGS] on the same 200 instances of basic Kuratowskian graphs with random ternary weights $J_{ij} \in \{-1, 0, +1\}$, with instances divided equally between graph sizes $N = 64$ and $N = 144$. In all cases, the matrix weight elements are drawn from the discrete probability mass function given by Eq. (15) with $p = 0.1$. (b) Violin plots demonstrate the distribution of CVGA's quality improvement performance compared with the best solution found by any competing method across the $N = 64$ and $N = 144$ basic Kuratowskian graph instances.

proximity gap metric to evaluate performance. The proximity gap provides a measure of the distance between any solution state and the best-known state by comparing their objective values. More precisely, it is defined as the ratio of the objective value obtained by a given method to the best objective value found among all methods. Here the objective value is given by the XY Hamiltonian H_{XY}. When comparing optimization methods on basic Kuratowskian graphs, we choose $p = 0.1$, the hardest value of p, which is the probability that a coupling is set to zero. From Fig. 3(c), we see that this occurs when $p = 0.1$, where the average sample variance s^2 of Kuramoto runs is maximized.

Figure 7(a) compares the objective values obtained by CVGA with those obtained by one-dimensional Stuart-Landau, SVL, Kuramoto, and BFGS methods for $N = 64$ and $N = 144$ basic Kuratowskian graphs. We define the quality improvement of CVGA over another method X in terms of objective values O as $(O_X - O_{\mathrm{CVGA}})/O_{\mathrm{CVGA}}$, showcasing these metrics in Fig. 7(b), where X represents the best-performing competing method for each instance.

These results demonstrate that CVGA consistently achieves ground states more reliably than one-dimensional models, particularly in larger and more complex systems.

V. CONCLUSIONS

We have presented CVGA, a gain-based analog computing scheme for minimizing XY Hamiltonians on challenging graph structures. CVGA combines multidimensional continuous spin variables, soft-amplitude annealing, and a uniform four-body locking penalty to reshape the effective energy landscape. By exploiting a higher-dimensional vector representation, it enhances phase mobility, allowing the dynamics to circumvent barriers that trap one-dimensional models and thereby increasing the probability of reaching true ground states.

These results suggest a route toward more powerful continuous analog optimization machines. Implementation of dimensionality-annealing strategies in analog spin platforms, such as laser networks, polariton condensates, and integrated photonic circuits, offers a promising pathway to ultrafast, energy-efficient computation with accurate ground-state recovery, and represents a promising step forward in the design of physics-inspired optimizers.

As an outlook, we note that although CVGA is a purely classical dissipative annealer, its use of higher-dimensional soft degrees of freedom together with a time-dependent locking penalty bears a conceptual resemblance to the role of noncommuting driver terms in quantum annealing. One could, in principle, formulate a quantum rotor analogue with two angular variables per site and a locking interaction similar to H_3, and study how its instantaneous spectrum and adiabatic gap behave, but such an analysis lies beyond the present work. Exploring whether CVGA-inspired embeddings and penalty structures can inform the design of future quantum annealing architectures is therefore an interesting direction for future research.

ACKNOWLEDGMENTS

J.S.C. acknowledges Ph.D. support from EPSRC (Grant No. EP/T517847/1). N.G.B. acknowledges support from the HORIZON EIC-2022-PATHFINDERCHALLENGES-01 HEISINGBERG Project 101114978, the EPSRC UK Multidisciplinary Centre for Neuromorphic Computing (Grant No. UKRI982), and the Weizmann UK Making Connections program (Grant No. 142568).

DATA AVAILABILITY

The data that support the findings of this study are available from the first author upon reasonable request.

APPENDIX A: COMPLEX GINZBURG-LANDAU EQUATION

Gain-based models that describe the dynamics of complex oscillators ψ_i are based on physical implementations of laser or nonequilibrium condensate networks coupled to a reservoir n_{R}. The systems are described by the generalized complex Ginzburg-Landau equation

$$i\dot{\psi}_i = -\nabla^2\psi_i + |\psi_i|^2\psi_i + g n_{\mathrm{R}}\psi_i + i(n_{\mathrm{R}} - 1)\psi_i, \quad \text{(A1)}$$

with reservoir dynamics $\dot{n}_{\mathrm{R}} = -(b_0 + b_1|\psi_i|^2)n_{\mathrm{R}} + P_i$, where g, b_0, and b_1 are dimensionless parameters, and

P_i is the pumping intensity. Networks of oscillators are constructed by coupling multiple lasers or condensates. In this case, with use of the tight-binding approximation from the mean-field complex Ginzburg-Landau equation, or the mean-field Maxwell-Bloch equations for laser cavities, Eq. (A1) becomes

$$\dot{\psi}_i = -i|\psi_i|^2\psi_i - \psi_i + (1-ig)\left[R_i\psi_i + \alpha\sum_{j\neq i} J_{ij}\psi_j\right], \tag{A2}$$

where R_i is the ith reservoir density, which follows the dynamics $\dot{R}_i = b_0(\gamma_i - R_i - \xi R_i|\psi_i|^2)$, where $\xi = b_1/b_0$, γ_i is the effective pumping rate and α quantifies the overall strength of coupling, and J_{ij} is the individual coupling strength between the ith and jth oscillators. In the fast reservoir relaxation limit, $b_0 \gg 1$, and the reservoir dynamics can be replaced with its steady-state $R_i = \gamma_i/(1+\xi|\psi_i|^2)$ to lead to a Stuart-Landau network [Eq. (1)] of coupled oscillators. For lasers, the nonlinear self-interactions given by the first term on the right-hand side of Eq. (A2) are zero.

APPENDIX B: FROM *XY* TO ISING IN GAIN-BASED SOLVERS

To obtain the minimum of the Ising Hamiltonian using Eq. (1), a mechanism is required to restrict phases to $\theta_i \in \{0,\pi\}$. This may be achieved in many ways, for instance, by coupling the real parts of the field in the coupling term of Eq. (1) as $J_{ij}(\psi_j + \psi_j^*)$. Then the phases θ_i will automatically be projected onto 0 or π [36]. Or it may be achieved by externally forcing the system at a frequency resonant with the frequency of the coherent state such that $h(t)\psi^{*(q-1)}$ is added to the right-hand side of Eq. (1), where $h(t)$ is the real time-dependent magnitude of the resonant pumping term. The presence of this external forcing produces q solutions whose phases differ by $2\pi/q$ [39]. For $q > 2$, the network emulates the q-state Potts model with phases restricted to discrete values that are multiples of $2\pi/q$. Minimizing the Ising Hamiltonian, therefore, requires taking $q = 2$. For sufficiently large $h(t)$, a feasible Ising solution is obtained by penalizing phases that are not equal to 0 or π.

APPENDIX C: MÖBIUS LADDER GRAPHS FOR *XY* NETWORKS

Möbius ladder graphs are cyclic graphs with an even number of vertices. They can be visualized as nodes arranged in a ring with antiferromagnetic circle couplings $J_{ij} = -1$ between nearest neighbors, and variable cross-circle couplings $J_{ij} = -J$ between diametrically opposite vertices. At some critical value $J = J_{\text{crit}}$, the ground-state configuration changes. We denote these states as S_0 and S_1, respectively. Notably, below and above $J = J_e = 1 - \cos(2\pi/N)$, the leading eigenvalue of the coupling matrix $\mathbf{J}$ changes from S_0 to S_1, where for Ising spins $J_{\text{crit}} \neq J_e$. Ising Hamiltonian minimization on Möbius ladder graphs is known to be computationally difficult for certain parameter regimes [37]. Specifically, for cross-circle couplings $J_e < J < J_{\text{crit}}$, many physically inspired optimization algorithms fail to recover the ground state with high probability [38]. This originates from the behavior of $\mathbf{J}$, where for $J_e < J < J_{\text{crit}}$, the eigenvector of the principal eigenvalue does not correspond to the Ising ground state. Figure 8(a) illustrates how these eigenvalues vary as a function of J.

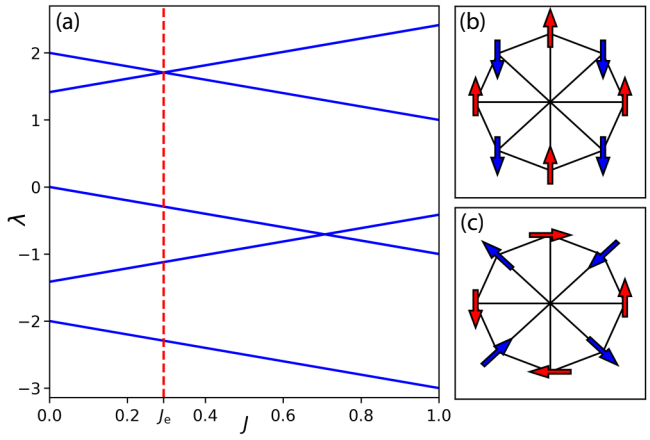


FIG. 8. (a) Eigenvalues of an $N = 8$ Möbius ladder graph as a function of J. J_e, illustrated by the vertical dashed red line, is the point at which the two largest eigenvalues cross. XY ground states correspond to $S_{XY}^{(0)}$ for $J < J_{\text{crit}}$ and $S_{XY}^{(1)}$ for $J > J_{\text{crit}}$, where $J_{\text{crit}} = J_e$ for the XY model. XY spin configurations for (b) $S_{XY}^{(0)}$ and (c) $S_{XY}^{(1)}$.

Similarly to for the Ising model, in the continuous XY regime, there are two distinct ground states as J is varied; namely, $S_{XY}^{(0)}$ for $J < J_{\text{crit}}$ and $S_{XY}^{(1)}$ for $J > J_{\text{crit}}$. These have Hamiltonians $H_{XY}^{(0)} = (J-2)N/2$ and $H_{XY}^{(1)} = [2\cos((N-2)\pi/N) - J]N/2$, respectively, and are shown in Figs. 8(b) and 8(c). The critical value J_{crit} at which these energies intercept is given by $J_{\text{crit}} = 1 - \cos(2\pi/N)$. This is exactly equal to J_e—the point at which the leading eigenvalues intercept one another. Therefore, in the XY regime, $J_e = J_{\text{crit}}$, and the eigenvectors of the principal eigenvalues correspond to the ground-state solutions overall J. Thus, in the XY model the Möbius ladder ground state can be obtained directly from the spectrum of J, making the instance analytically simple. Nevertheless, its energy landscape still supports domain-wall excitations with small ground-state basins, so we include the 4-regular Möbius ladder among our benchmarks in Sec. III, alongside more strongly frustrated graphs. Specifically, in Sec. III we use frustration and the promotion of domain boundaries to devise suitably hard graphs.

APPENDIX D: CIRCULANT GRAPHS

The weighted adjacency matrix **J** of a 4-regular Möbius ladder graph is circulant because it is constructed through cyclical permutations of any N-vector. The graph inherently has vertex permutation symmetry, signifying boundary periodicity and uniform neighborhoods. Any circulant matrix can be expressed as a polynomial of a shift matrix **P**. For 4-regular Möbius ladder graphs

$$\mathbf{J} = -\mathbf{P} - \mathbf{P}^2 - \mathbf{P}^{N-2} - \mathbf{P}^{N-1}, \tag{D1}$$

where **P** is the $N \times N$ canonical shift matrix $\mathbf{P} = \left(\begin{smallmatrix} \mathbf{0} & \mathbf{I} \\ 1 & \mathbf{0} \end{smallmatrix}\right)$, where **I** is an $(N-1) \times (N-1)$ identity matrix. The structure of a circulant matrix is contained in any row, and its eigenvalues and eigenvectors can be analytically derived with use of the N roots of unity of a polynomial $\omega = \exp(2\pi i/N)$, where the row components **c** of the matrix **J** act as coefficients. The eigenvectors of **J** are the same as the shift matrix **P**, while the N eigenvalues λ_n are the components of the product **Fc**, where **F** is the $N \times N$ Fourier matrix. This gives the eigenvalues as

$$\begin{aligned} \lambda_n &= -\omega^n - \omega^{2n} - \omega^{(N-2)n} - \omega^{(N-1)n} \\ &= -4\cos(\pi n/N)\cos(3\pi n/N) \end{aligned} \tag{D2}$$

for $n = 0, 1, \ldots, N-1$. The dominant modes are low-frequency Fourier modes; for certain N these resemble short-period patterns. The eigenvectors of **J** form an orthogonal basis, and since $\lambda_n \in \mathbb{R}$ and $\mathbf{J} \in \mathbb{R}^{N\times N}$, we can always choose the eigenvectors to be real. In this case, the eigenvectors corresponding to the eigenvalues with index n are

$$\mathbf{q}_n = \frac{1}{2}\begin{pmatrix} 2 \\ \omega^n + \omega^{-n} \\ \omega^{2n} + \omega^{-2n} \\ \vdots \\ \omega^{(N-1)n} + \omega^{-(N-1)n} \end{pmatrix} = \begin{pmatrix} 1 \\ \cos\left(\frac{2\pi n}{N}\right) \\ \cos\left(\frac{4\pi n}{N}\right) \\ \vdots \\ \cos\left(\frac{2(N-1)\pi n}{N}\right) \end{pmatrix}. \tag{D3}$$

This is the ground-state solution of the 4-regular Möbius ladder graph when each component of the eigenvector is associated with the cosine of the phase. Graphs with circulant coupling matrices are realizable in current experimental platforms [44,46,47]. This, combined with the accessibility to the analytical energy spectrum they allow, makes them natural platforms for analyzing and contrasting properties of different platforms.

APPENDIX E: MATERIALS AND METHODS

In all comparisons between the methods presented in this paper, numerical integration is performed by the fourth-order Runge-Kutta scheme with discrete time step $\Delta t = 0.1$. For CVGA, a linear annealing schedule is chosen such that $P(t) = \beta t$. Each time evolution is to a maximum time $T = 1000$. The total parameter space for CVGA is $\{\varepsilon, \alpha, \beta, \gamma(0)\}$, with optimal choices deduced by the PYTHON machine-learning online optimization package `M-LOOP` [51]. The hyperparameter α is scaled by the inverse of the largest positive eigenvalue of the coupling matrix **J** such that $\alpha = \alpha'/\lambda_{\max}$, and the initial effective gain $\gamma_i(0) = \gamma(0)$ for all i. For a selection of graph sizes for 4-regular Möbius ladder graphs, triangular lattice graphs, and basic Kuratowskian graphs, the optimal parameter choices are detailed in Table I. Since the value of $\lambda_{\max}$ varies for random instances of basic Kuratowskian graphs, the values of α' in Table I for this case are chosen as the best over a sample of 100 $p = 0.1$ graph instances.

For results obtained with the one-dimensional Stuart-Landau network given by Eq. (1), the values of the parameters ε, α, and $\gamma(0)$ are taken from Table I. For the SVL model, we fix $m = 1.0$ and $b = 0.9$, and the Gaussian noise ξ is sampled from $N(0, 0.1)$. The Kuramoto model is implemented without hyperparameters, given by Eq. (6) with $\alpha = 1$. The BFGS algorithm is run with the `SciPy` library using the `scipy.optimize.minimize` function.

Our goal in choosing these parameters is to provide representative and physically reasonable dynamics, not to perform a full hyperparameter optimization for each solver. In particular, the one-dimensional Stuart-Landau network shares the same gain dynamics as CVGA, and we deliberately use the same ϵ, α, and $\gamma(0)$ so that the impact of the additional vector component and penalty H_3 can be assessed under identical conditions. For the Kuramoto model, the constant prefactor α can be absorbed into a rescaling of time in Eq. (6), so taking $\alpha = 1$ and integrating Eq. (6) to a fixed time horizon T is sufficient once convergence is ensured. The SVL model parameters (m, b, σ) are chosen within the regime used in Ref. [52] for XY-type problems, rather than tuned per instance. A

TABLE I. Optimal sets of hyperparameters for different graphs and sizes.

Graph type	N	ε	α'	β	$\gamma(0)$
4-regular Möbius	12	0.032	2.882	0.020	−0.139
	102	0.022	2.402	0.003	−0.453
	204	0.002	2.529	0.008	−1.235
Triangular	16	0.045	1.129	0.018	−0.900
	100	0.034	2.280	0.004	−0.526
	196	0.010	1.301	0.005	−0.986
Kuratowskian	16	0.047	1.148	0.016	−0.295
	64	0.023	2.763	0.007	−1.275
	144	0.012	2.745	0.014	−1.285

systematic time-to-solution optimization over all hyperparameters for all methods is therefore beyond the present scope and would constitute a separate benchmark study.

The hyperparameters used for CVGA in Table I correspond to dimensionless quantities that naturally arise in gain-based photonic and polaritonic implementations. The characteristic time unit in such systems is the cavity photon lifetime or reservoir relaxation time; in lasers this ranges from 1 to 100 ps and in polariton condensates from 0.1 to 10 ns. Our chosen annealing length $T = 1000$ therefore corresponds to 10^2–10^4 such time units, consistent with experimentally standard pump-ramp durations. The regulation strength $\epsilon \in [10^{-3}, 10^{-1}]$ matches the typical ratios of nonlinear saturation to linear gain in Stuart-Landau reductions of the complex Ginzburg-Landau and Maxwell-Bloch equations (Appendix A). Similarly, the initial gain $\gamma(0) \in [-1.3, -0.1]$ represents underthreshold pumping routinely used in optical and polaritonic simulators. The coupling coefficient $\alpha = \alpha'/\lambda_{\max}$ is normalized with use of the largest eigenvalue of the coupling matrix, and corresponds physically to intersite feedback strengths on the order of the cavity linewidth. These ranges are consistent with the experimentally realized operating regimes reported in Refs. [11,13,14,16,44].

APPENDIX F: TOY EXAMPLE OF BARRIER REDUCTION ON A FRUSTRATED TRIANGLE

Here we illustrate CVGA's barrier-reduction mechanism on the smallest frustrated XY instance, a single antiferromagnetic triangle, complementing the discussion in Sec. IV.

Consider three XY spins $\{\theta_1, \theta_2, \theta_3\}$ on the vertices of a triangle with antiferromagnetic couplings $J_{ij} = -1$ on each edge. Up to an overall constant and a choice of energy units, the XY energy [see Eq. (10) with unit amplitudes $r_i^{(1)} = r_i^{(2)} = 1$ and $J_{ij} = -1$] can be written as

$$H_{XY}(\boldsymbol{\theta}) = \sum_{(i,j)\in L} \cos(\theta_i - \theta_j), \quad L = \{(1,2),(2,3),(3,1)\}. \tag{F1}$$

Using the global U(1) symmetry, we set $\theta_1 = 0$ and write $\theta_2 = a$, $\theta_3 = b$. Then

$$H_{XY}(a,b) = \cos a + \cos b + \cos(a-b). \tag{F2}$$

Stationary points satisfy

$$\begin{aligned} \frac{\partial H_{XY}}{\partial a} &= -\sin a - \sin(a-b) = 0, \\ \frac{\partial H_{XY}}{\partial b} &= -\sin b + \sin(a-b) = 0. \end{aligned} \tag{F3}$$

One readily checks that

$$(a,b) = \left(\frac{2\pi}{3}, \frac{4\pi}{3}\right), \qquad (a,b) = \left(-\frac{2\pi}{3}, -\frac{4\pi}{3}\right) \tag{F4}$$

solve these equations and are minima. Evaluation of Eq. (F2) gives the ground-state energy

$$E_0 = H_{XY}\left(\frac{2\pi}{3}, \frac{4\pi}{3}\right) = H_{XY}\left(-\frac{2\pi}{3}, -\frac{4\pi}{3}\right) = -\frac{3}{2}. \tag{F5}$$

The chirality of the triangle is defined as

$$C(\boldsymbol{\theta}) = \sin(\theta_2 - \theta_1) + \sin(\theta_3 - \theta_2) + \sin(\theta_1 - \theta_3). \tag{F6}$$

In the gauge $\theta_1 = 0$ this becomes

$$C(a,b) = \sin a + \sin(b-a) - \sin b. \tag{F7}$$

Using the trigonometric identity for $x + y + z = 0$,

$$\sin x + \sin y + \sin z = 4 \sin\frac{x+y}{2} \sin\frac{y+z}{2} \sin\frac{z+x}{2},$$

and setting $x = a$, $y = b - a$, and $z = -b$, we obtain

$$C(a,b) = -4 \sin\frac{a}{2} \sin\frac{b}{2} \sin\frac{a-b}{2}. \tag{F8}$$

The two ground states in Eq. (F4) have opposite chirality, $C = \pm C_0$, with $C_0 > 0$. From Eq. (F8) we see that

$$\begin{aligned} C(a,b) = 0 \quad &\Longleftrightarrow \quad \sin\frac{a}{2} = 0 \\ \text{or } \sin\frac{b}{2} = 0 \quad &\text{or } \sin\frac{a-b}{2} = 0, \end{aligned} \tag{F9}$$

i.e., $a \equiv 0$, $b \equiv 0$, or $a \equiv b \pmod{2\pi}$. In each case at least two of the three spins are collinear. For instance, when $a = 0$, we have $\theta_1 = \theta_2 = 0$, $\theta_3 = b$, and

$$H_{XY}(0,b) = \cos 0 + \cos b + \cos(-b) = 1 + 2\cos b, \tag{F10}$$

whose minimum is

$$H_{XY}(0,\pi) = -1. \tag{F11}$$

The other cases, $b = 0$ and $a = b$, lead to the same minimal value -1. Thus, among all configurations with zero

chirality ($C = 0$) the lowest possible energy is

$$\min_{C(a,b)=0} H_{XY}(a,b) = -1. \tag{F12}$$

Now consider any continuous path

$$t \mapsto (\theta_1(t), \theta_2(t), \theta_3(t)), \qquad t \in [0,1],$$

connecting the two chiral ground states, e.g.,

$$\begin{aligned}(\theta_1(0), \theta_2(0), \theta_3(0)) &= \left(0, \frac{2\pi}{3}, \frac{4\pi}{3}\right),\\ (\theta_1(1), \theta_2(1), \theta_3(1)) &= \left(0, -\frac{2\pi}{3}, -\frac{4\pi}{3}\right).\end{aligned} \tag{F13}$$

Along this path the chirality $C(t) \equiv C(\boldsymbol{\theta}(t))$ is continuous with $C(0) = +C_0$ and $C(1) = -C_0$, so by the intermediate value theorem there exists $t_* \in (0,1)$ with $C(t_*) = 0$. At that point, Eq. (F12) implies

$$H_{XY}(\boldsymbol{\theta}(t_*)) \geq -1. \tag{F14}$$

Therefore, any continuous path between the two chiral ground states must cross an energy barrier of at least

$$\begin{aligned}\Delta E_{XY} &:= \inf_{\text{paths}} \left[\max_t H_{XY}(\boldsymbol{\theta}(t)) - E_0\right]\\ &\geq (-1) - \left(-\frac{3}{2}\right) = \frac{1}{2}.\end{aligned} \tag{F15}$$

In the scalar XY model this barrier height is set by the interaction scale and cannot be tuned without changing the problem Hamiltonian itself.

We now show how the same frustrated triangle behaves under the CVGA construction, focusing on the phase degrees of freedom and assuming that the amplitudes have relaxed to unity. The effective phase Hamiltonian obtained from Eqs. (10) and (12) is

$$\begin{aligned}&H_{\triangle}(\boldsymbol{\theta}^{(1)}, \boldsymbol{\theta}^{(2)}; P)\\ &\quad= \sum_{(i,j)\in L} \left[\cos\left(\theta_i^{(1)} - \theta_j^{(1)}\right) + \cos\left(\theta_i^{(2)} - \theta_j^{(2)}\right)\right]\\ &\qquad - 2P \sum_{(i,j)\in L} \cos\left[\left(\theta_i^{(1)} - \theta_j^{(1)}\right) - \left(\theta_i^{(2)} - \theta_j^{(2)}\right)\right],\end{aligned} \tag{F16}$$

where $L = \{(1,2),(2,3),(3,1)\}$ and $P \geq 0$ is the magnitude of the locking penalty. For this toy example we have restricted the sums in Eq. (12) to the three edges L of the triangle; this simplification only rescales the effective coefficient P by an overall constant and does not affect the conclusion that the relevant barrier scale is $O(P)$. Let $\boldsymbol{\theta}^+$ and $\boldsymbol{\theta}^-$ denote the two chiral ground-state configurations of the scalar triangle,

$$\boldsymbol{\theta}^+ = \left(0, \frac{2\pi}{3}, \frac{4\pi}{3}\right), \qquad \boldsymbol{\theta}^- = \left(0, -\frac{2\pi}{3}, -\frac{4\pi}{3}\right), \tag{F17}$$

so $H_{XY}(\boldsymbol{\theta}^{\pm}) = E_0 = -3/2$. We now evaluate Eq. (F16) on the four configurations in which each CVGA component sits in a scalar ground state:

$$(++): \quad \boldsymbol{\theta}^{(1)} = \boldsymbol{\theta}^+, \boldsymbol{\theta}^{(2)} = \boldsymbol{\theta}^+, \tag{F18}$$

$$(--): \quad \boldsymbol{\theta}^{(1)} = \boldsymbol{\theta}^-, \boldsymbol{\theta}^{(2)} = \boldsymbol{\theta}^-, \tag{F19}$$

$$(+-): \quad \boldsymbol{\theta}^{(1)} = \boldsymbol{\theta}^+, \boldsymbol{\theta}^{(2)} = \boldsymbol{\theta}^-, \tag{F20}$$

$$(-+): \quad \boldsymbol{\theta}^{(1)} = \boldsymbol{\theta}^-, \boldsymbol{\theta}^{(2)} = \boldsymbol{\theta}^+. \tag{F21}$$

For both $(++)$ and $(--)$, the bond phase differences in the two components are identical, so $\theta_{ij}^{(1)} - \theta_{ij}^{(2)} = 0$ for all $(i,j) \in L$, and hence $\cos(\theta_{ij}^{(1)} - \theta_{ij}^{(2)}) = 1$. Using $H_{XY}(\boldsymbol{\theta}^{\pm}) = E_0$ and $|L| = 3$, we obtain

$$H_{\triangle}^{++}(P) = H_{\triangle}^{--}(P) = E_0 + E_0 - 2P \sum_{(i,j)\in L} 1 = -3 - 6P. \tag{F22}$$

For the mixed configurations $(+-)$ and $(-+)$, each component separately is in a scalar ground state, so the first sum in Eq. (F16) still yields $E_0 + E_0 = -3$. However, the bond phase differences now have opposite chirality. If we denote the ground-state bond differences in the $+$ state by

$$\theta_{12}^+ = -\frac{2\pi}{3}, \quad \theta_{23}^+ = -\frac{2\pi}{3}, \quad \theta_{31}^+ = \frac{4\pi}{3},$$

those in the $-$ state are their negatives, $\theta_{ij}^- = -\theta_{ij}^+$. Therefore, for the mixed configuration $(+-)$,

$$\theta_{ij}^{(1)} - \theta_{ij}^{(2)} = \theta_{ij}^+ - \theta_{ij}^- = 2\theta_{ij}^+,$$

so

$$\cos\left(\theta_{ij}^{(1)} - \theta_{ij}^{(2)}\right) = \cos(2\theta_{ij}^+) = \cos\left(\frac{4\pi}{3}\right) = -\frac{1}{2}$$

for each of the three bonds. Thus,

$$\begin{aligned}H_{\triangle}^{+-}(P) = H_{\triangle}^{-+}(P) &= E_0 + E_0 - 2P \sum_{(i,j)\in L} \left(-\frac{1}{2}\right)\\ &= -3 + 3P.\end{aligned} \tag{F23}$$

Equations (F22) and (F23) show that for every fixed $P > 0$, the co-chiral configurations $(++)$ and $(--)$ are degenerate global minima of the reduced CVGA triangle with

energy

$$E^{\mathrm{GS}}_{\mathrm{CVGA}}(P) = -3 - 6P, \tag{F24}$$

while the mixed configurations $(+-)$ and $(-+)$ are the first excited states with energy

$$E^{\mathrm{mix}}_{\mathrm{CVGA}}(P) = -3 + 3P. \tag{F25}$$

The energy splitting between these locally stable minima is therefore given by

$$\Delta E_{\mathrm{CVGA}}(P) = E^{\mathrm{mix}}_{\mathrm{CVGA}}(P) - E^{\mathrm{GS}}_{\mathrm{CVGA}}(P) = 9P. \tag{F26}$$

For the scalar XY triangle, the minimal barrier height between the two chiral ground states is bounded below by $\Delta E_{XY} \geq 1/2$ [Eq. (F15)], and this barrier is set by the fixed interaction scale of the problem. In the reduced CVGA model, the states in which the two components carry opposite chiralities are exact ground states of the problem term H_2 in each replica, and their excess energy over the co-chiral global minima is entirely due to the locking penalty H_3, scaling linearly with the annealing parameter P via Eq. (F26). Any CVGA trajectory that interpolates between the co-chiral minima $(++)$ and $(--)$ can therefore flip chirality by passing through such mixed-chirality states, so the relevant barrier along this path is set by $\Delta E_{\mathrm{CVGA}}(P)$. During the early stages of the CVGA protocol, when $P(t)$ is small, the energy cost of configurations with opposite chiralities in the two components is therefore only $\mathcal{O}(P(t))$, which can be made parametrically smaller than the intrinsic scalar barrier $1/2$. In other words, the additional vector degree of freedom allows the system to explore configurations that remain at the XY ground-state energy in each replica, while moving the barrier between competing chiral sectors into a controllable penalty term. This toy example makes explicit how CVGA relocates the relevant barriers from the fixed problem Hamiltonian into a tunable part of the dynamics, a mechanism that underlies the enhanced ground-state recovery observed on larger frustrated graphs.

[1] M. W. Johnson, M. H. Amin, S. Gildert, T. Lanting, F. Hamze, N. Dickson, R. Harris, A. J. Berkley, J. Johansson, P. Bunyk *et al.*, Quantum annealing with manufactured spins, Nature **473**, 194 (2011).

[2] V. S. Denchev, S. Boixo, S. V. Isakov, N. Ding, R. Babbush, V. Smelyanskiy, J. Martinis, and H. Neven, What is the computational value of finite range tunneling? Phys. Rev. X **6**, 031015 (2016).

[3] F. Arute, K. Arya, R. Babbush, D. Bacon, J. C. Bardin, R. Barends, R. Biswas, S. Boixo, F. G. Brandao, D. A. Buell *et al.*, Quantum supremacy using a programmable superconducting processor, Nature **574**, 505 (2019).

[4] P. L. McMahon, A. Marandi, Y. Haribara, R. Hamerly, C. Langrock, S. Tamate, T. Inagaki, H. Takesue, S. Utsunomiya, K. Aihara *et al.*, A fully programmable 100-spin coherent Ising machine with all-to-all connections, Science **354**, 614 (2016).

[5] T. Inagaki, Y. Haribara, K. Igarashi, T. Sonobe, S. Tamate, T. Honjo, A. Marandi, P. L. McMahon, T. Umeki, K. Enbutsu *et al.*, A coherent Ising machine for 2000-node optimization problems, Science **354**, 603 (2016).

[6] Y. Yamamoto, K. Aihara, T. Leleu, K.-I. Kawarabayashi, S. Kako, M. Fejer, K. Inoue, and H. Takesue, Coherent Ising machines—Optical neural networks operating at the quantum limit, npj Quantum Inf. **3**, 1 (2017).

[7] T. Honjo, T. Sonobe, K. Inaba, T. Inagaki, T. Ikuta, Y. Yamada, T. Kazama, K. Enbutsu, T. Umeki, and R. Kasahara, 100,000-spin coherent Ising machine, Sci. Adv. **7**, eabh0952 (2021).

[8] T. Honjo, K. Inaba, T. Inagaki, T. Ikuta, Y. Yamada, and H. Takesue, in *2022 IEEE 22nd International Conference on Nanotechnology (NANO)* (IEEE, Palma de Mallorca, Spain, 2022), pp. 405–408.

[9] F. Cai, S. Kumar, T. Van Vaerenbergh, X. Sheng, R. Liu, C. Li, Z. Liu, M. Foltin, S. Yu, Q. Xia *et al.*, Power-efficient combinatorial optimization using intrinsic noise in memristor Hopfield neural networks, Nat. Electron. **3**, 409 (2020).

[10] M. Babaeian, D. T. Nguyen, V. Demir, M. Akbulut, P.-A. Blanche, Y. Kaneda, S. Guha, M. A. Neifeld, and N. Peyghambarian, A single shot coherent Ising machine based on a network of injection-locked multicore fiber lasers, Nat. Commun. **10**, 3516 (2019).

[11] V. Pal, S. Mahler, C. Tradonsky, A. A. Friesem, and N. Davidson, Rapid fair sampling of the XY spin Hamiltonian with a laser simulator, Phys. Rev. Res. **2**, 033008 (2020).

[12] M. Parto, W. Hayenga, A. Marandi, D. N. Christodoulides, and M. Khajavikhan, Realizing spin Hamiltonians in nanoscale active photonic lattices, Nat. Mater. **19**, 725 (2020).

[13] D. Pierangeli, G. Marcucci, and C. Conti, Large-scale photonic Ising machine by spatial light modulation, Phys. Rev. Lett. **122**, 213902 (2019).

[14] C. Roques-Carmes, Y. Shen, C. Zanoci, M. Prabhu, F. Atieh, L. Jing, T. Dubček, C. Mao, M. R. Johnson, V. Čeperić *et al.*, Heuristic recurrent algorithms for photonic Ising machines, Nat. Commun. **11**, 249 (2020).

[15] K. Kim, M.-S. Chang, S. Korenblit, R. Islam, E. E. Edwards, J. K. Freericks, G.-D. Lin, L.-M. Duan, and C. Monroe, Quantum simulation of frustrated Ising spins with trapped ions, Nature **465**, 590 (2010).

[16] N. G. Berloff, M. Silva, K. Kalinin, A. Askitopoulos, J. D. Töpfer, P. Cilibrizzi, W. Langbein, and P. G. Lagoudakis, Realizing the classical XY Hamiltonian in polariton simulators, Nat. Mater. **16**, 1120 (2017).

[17] K. P. Kalinin, A. Amo, J. Bloch, and N. G. Berloff, Polaritonic XY-Ising machine, Nanophotonics **9**, 4127 (2020).

[18] M. Vretenar, B. Kassenberg, S. Bissesar, C. Toebes, and J. Klaers, Controllable Josephson junction for photon Bose-Einstein condensates, Phys. Rev. Res. **3**, 023167 (2021).

[19] A. Litvinenko, R. Khymyn, R. Ovcharov, and J. Åkerman, A 50-spin surface acoustic wave Ising machine, Commun. Phys. **8**, 58 (2025).

[20] A. Lucas, Ising formulations of many NP problems, Front. Phys. **2**, 5 (2014).

[21] M. Yamaoka, C. Yoshimura, M. Hayashi, T. Okuyama, H. Aoki, and H. Mizuno, A 20k-spin Ising chip to solve combinatorial optimization problems with CMOS annealing, IEEE J. Solid-State Circuits **51**, 303 (2016).

[22] K. Tanahashi, S. Takayanagi, T. Motohashi, and S. Tanaka, Application of Ising machines and a software development for Ising machines, J. Phys. Soc. Jpn. **88**, 061010 (2019).

[23] A. Momeni, B. Rahmani, B. Scellier, L. G. Wright, P. L. McMahon, C. C. Wanjura, Y. Li, A. Skalli, N. G. Berloff, T. Onodera *et al.*, Training of physical neural networks, Nature **645**, 53 (2025).

[24] X. Guo, T. D. Barrett, Z. M. Wang, and A. Lvovsky, Backpropagation through nonlinear units for the all-optical training of neural networks, Photonics Res. **9**, B71 (2021).

[25] J. Spall, X. Guo, and A. Lvovsky, Training neural networks with end-to-end optical backpropagation, Adv. Photonics **7**, 016004 (2025).

[26] P. Freire, E. Manuylovich, J. E. Prilepsky, and S. K. Turitsyn, Artificial neural networks for photonic applications—From algorithms to implementation: Tutorial, Adv. Opt. Photonics **15**, 739 (2023).

[27] M. Gilli, D. Maringer, and E. Schumann, *Numerical Methods and Optimization in Finance* (Academic Press, Amsterdam, 2019).

[28] R. Z. Wang, J. S. Cummins, M. Syed, N. Stroev, G. Pastras, J. Sakellariou, S. Tsintzos, A. Askitopoulos, D. Veraldi, M. C. Strinati *et al.*, Efficient computation using spatial-photonic Ising machines with low-rank and circulant matrix constraints, Commun. Phys. **8**, 86 (2025).

[29] P. W. Anderson, in *Basic Notions of Condensed Matter Physics* (CRC Press, Boca Raton, 2018).

[30] P. Minnhagen, The two-dimensional Coulomb gas, vortex unbinding, and superfluid-superconducting films, Rev. Mod. Phys. **59**, 1001 (1987).

[31] W. H. Zurek, in *Formation and Interactions of Topological Defects: Proceedings of a NATO Advanced Study Institute on Formation and Interactions of Topological Defects* (Springer, New York, NY, 1995), pp. 349–378.

[32] P.-G. De Gennes and J. Prost, *The Physics of Liquid Crystals, 83* (Oxford University Press, Oxford, 1993).

[33] D. Gallina and G. Pastor, Disorder-induced transformation of the energy landscapes and magnetization dynamics in two-dimensional ensembles of dipole-coupled magnetic nanoparticles, Phys. Rev. X **10**, 021068 (2020).

[34] K. A. Dill, S. B. Ozkan, M. S. Shell, and T. R. Weikl, The protein folding problem, Annu. Rev. Biophys. **37**, 289 (2008).

[35] E. J. Candes, Y. C. Eldar, T. Strohmer, and V. Voroninski, Phase retrieval via matrix completion, SIAM Rev. **57**, 225 (2015).

[36] M. Syed and N. G. Berloff, Physics-enhanced bifurcation optimisers: All you need is a canonical complex network, IEEE J. Sel. Top. Quantum Electron. **29**, 1 (2023).

[37] J. S. Cummins, H. Salman, and N. G. Berloff, Ising Hamiltonian minimization: Gain-based computing with manifold reduction of soft spins vs quantum annealing, Phys. Rev. Res. **7**, 013150 (2025).

[38] J. S. Cummins and N. G. Berloff, Vector Ising spin annealer for minimizing Ising Hamiltonians, Commun. Phys. **8**, 225 (2025).

[39] K. P. Kalinin and N. G. Berloff, Global optimization of spin Hamiltonians with gain-dissipative systems, Sci. Rep. **8**, 17791 (2018).

[40] S. Abreu, I. Boikov, M. Goldmann, T. Jonuzi, A. Lupo, S. Masaad, L. Nguyen, E. Picco, G. Pourcel, A. Skalli *et al.*, A photonics perspective on computing with physical substrates, Rev. Phys., **12**100093 (2024).

[41] N. Stroev and N. G. Berloff, Discrete polynomial optimization with coherent networks of condensates and complex coupling switching, Phys. Rev. Lett. **126**, 050504 (2021).

[42] K. Kalinin, G. Mourgias-Alexandris, H. Ballani, N. G. Berloff, J. H. Clegg, D. Cletheroe, C. Gkantsidis, I. Haller, V. Lyutsarev, F. Parmigiani *et al.*, Analog Iterative Machine (AIM): using light to solve quadratic optimization problems with mixed variables, arXiv preprint arXiv:2304.12594.

[43] K. P. Kalinin, J. Gladrow, J. Chu, J. H. Clegg, D. Cletheroe, D. J. Kelly, B. Rahmani, G. Brennan, B. Canakci, F. Falck *et al.*, Analog optical computer for AI inference and combinatorial optimization, Nature **645**, 354 (2025).

[44] H. Ohadi, R. Gregory, T. Freegarde, Y. Rubo, A. Kavokin, N. Berloff, and P. Lagoudakis, Nontrivial phase coupling in polariton multiplets, Phys. Rev. X **6**, 031032 (2016).

[45] N. Stroev and N. G. Berloff, Programmable k-local Ising machines and all-optical Kolmogorov-Arnold networks on photonic platforms, arXiv preprint arXiv:2508.17440.

[46] M. C. Strinati, D. Pierangeli, and C. Conti, All-optical scalable spatial coherent Ising machine, Phys. Rev. Appl. **16**, 054022 (2021).

[47] A. B. Ayoub and D. Psaltis, High speed, complex wavefront shaping using the digital micro-mirror device, Sci. Rep. **11**, 18837 (2021).

[48] K. P. Kalinin and N. G. Berloff, Computational complexity continuum within Ising formulation of NP problems, Commun. Phys. **5**, 20 (2020).

[49] S. Istrail, Statistical mechanics, three-dimensionality and NP-completeness: I. Universality of intractability for the partition function of the Ising model across non-planar lattices, in *Proceedings of the Thirty-Second Annual ACM Symposium on Theory of Computing* (Association for Computing Machinery, New York, NY, 2000), pp. 87–96.

[50] T. F. Rønnow, Z. Wang, J. Job, S. Boixo, S. V. Isakov, D. Wecker, J. M. Martinis, D. A. Lidar, and M. Troyer, Defining and detecting quantum speedup, Science **345**, 420 (2014).

[51] P. B. Wigley, P. J. Everitt, A. van den Hengel, J. W. Bastian, M. A. Sooriyabandara, G. D. McDonald, K. S. Hardman, C. D. Quinlivan, P. Manju, C. C. Kuhn *et al.*, Fast machine-learning online optimization of ultra-cold-atom experiments, Sci. Rep. **6**, 25890 (2016).

[52] D. Subires, F. J. Gómez-Ruiz, A. Ruiz-García, D. Alonso, and A. Del Campo, Benchmarking quantum annealing dynamics: The spin-vector Langevin model, Phys. Rev. Res. **4**, 023104 (2022).

[53] R. Hamerly, T. Inagaki, P. L. McMahon, D. Venturelli, A. Marandi, T. Onodera, E. Ng, C. Langrock, K. Inaba, T.

Honjo *et al.*, Experimental investigation of performance differences between coherent Ising machines and a quantum annealer, Sci. Adv. **5**, eaau0823 (2019).

[54] M. P. Harrigan, K. J. Sung, M. Neeley, K. J. Satzinger, F. Arute, K. Arya, J. Atalaya, J. C. Bardin, R. Barends, S. Boixo *et al.*, Quantum approximate optimization of non-planar graph problems on a planar superconducting processor, Nat. Phys. **17**, 332 (2021).

[55] F. Böhm, G. Verschaffelt, and G. Van der Sande, A poor man's coherent Ising machine based on opto-electronic feedback systems for solving optimization problems, Nat. Commun. **10**, 3538 (2019).